The Astrophysical Journal, 1009:201 (12pp), 2026 October 1 https://doi.org/10.3847/1538-4357/aea15a
© 2026. The Author(s). Published by the American Astronomical Society.
OPEN ACCESS

Morphology of Solar Filaments during the Solar Maximum of Cycle 24: A Study of 35 Filaments Focusing on Chirality, Barb Orientation, Skewness, and Eruptive Behavior

P. T. Jain Jacob[1,2] and Ram Ajor Maurya[1]
[1] Department of Physics, National Institute of Technology Calicut, Kozhikode-673601, India
[2] Indian Institute of Astrophysics, Bangalore-560034, India
Received 2025 April 17; revised 2026 August 17; accepted 2026 August 27; published 2026 September 29

Abstract

Filaments in the solar atmosphere are plasma structures held aloft by magnetic fields, counteracting the pull of gravity. Analyzing their magnetic structure is challenging due to the lack of direct observations of their magnetic fields. However, through multiwavelength intensity observations, one can infer their morphology. We identified 35 solar filaments during the maximum period of solar cycle 24. In order to ascertain their chirality, we analyzed Hα intensity observations. Using coronal ultraviolet intensity images, we also determined the skewness of the related coronal arcades. Furthermore, based on adjacent active regions, we classified filaments as quiescent or active according to the strength of nearby photospheric magnetic fields. We followed every filament over time to estimate their characteristics. The hemispheric chirality preference is followed by 27 (77%) filaments across all categories, based on observed bearing sense. We examined the skewness of the coronal arcades connected to 19 filaments, and they all complied with the hemisphere helicity criterion. The morphology of 16 filaments was also ascertained by integrating the skewness and bearing sense. There were 2 filaments with a sheared arcade morphology and 14 with a flux rope shape. Additionally, by analyzing the changes in the skewness of coronal arcades and the bearing sense of filament barbs over time, we examined the variation in the filament's magnetic structure. Further, we examined the temporal evolution of selected filaments that exhibit peculiar characteristics during the observational period. Lastly, we investigated the eruptive characteristics of these filaments. We did not find filaments that are more likely to explode because they do not adhere to the hemispheric chirality preference.

Unified Astronomy Thesaurus concepts: Solar filaments (1495); Solar prominences (1519); Solar magnetic fields (1503)

Materials only available in the online version of record: animation

1. Introduction

In the solar corona, filaments are dark, thread-like structures that are cooler and denser than the surrounding corona. These filaments, held up by the magnetic fields against the Sun's gravity, have their origins in the chromosphere and photosphere. As they reach the solar limb due to solar rotation, they manifest as prominences, bright features visible against the the sky. The spine of the filament represents the region of colder plasma suspended along the horizontal magnetic field. This structure is aligned with the polarity inversion line (PIL), where the line-of-sight component of photospheric magnetic field vanishes. The minor polarity regions on either side of the PIL connect to the filament spine, forming filament barbs, which also appear dark. Understanding the structure and behavior of filaments is critical, as these features play a significant role in solar activity, and studying them further could provide insights into their dynamic nature and eruptive behavior.

Recent studies have explored the morphology of filaments and their associated magnetic structures using both by observations and simulations. For example, S. F. Martin et al. (1994) and S. F. Martin (1998) used their wire model to illustrate the field lines of the filament spine and barbs, while P. C. Liewer et al. (2012) used stereoscopic techniques to observe these field lines from multiple angles. Filaments exhibit two distinct magnetic configurations: sheared arcade, where the filament's axial magnetic field almost aligns with the photospheric field, and flux rope, where the axial magnetic field is opposite (D. H. Mackay et al. 2010). In other words, a filament has normal polarity in the sheared arcade model and inverse polarity in the flux rope model. Inverse arcades and normal flux ropes, which are infrequently found in the solar atmosphere, are also thought to be potential magnetic structures (S. E. Gibson 2018). Understanding these magnetic configurations is essential for accurate filament classification and prediction of their eruptive behaviors. Furthermore, a sheared arcade and flux rope, which resemble normal and inverse polarity kinds, respectively, can be used to mimic a filament's magnetic structure (P.-F. Chen et al. 2014). High-resolution magnetic field studies on coronal features or the extrapolation of the photospheric magnetic field are further needed to disclose specifics about their magnetic architecture. Determining filament properties is hampered by the high computing cost of extrapolation and sporadic observations of the coronal magnetic field.

Simulation has played a pivotal role in interpreting the formation and magnetic structure of filaments. C. R. DeVore & S. K. Antiochos (2000) demonstrated that sheared magnetic arcades form as a result of shearing motions at the photospheric footpoints, especially near the PIL. These sheared fields lead to magnetic flux cancellations, which contribute to the formation of helical magnetic field lines, forming the foundation of the flux rope model (A. A. Van Ballegooijen &

Original content from this work may be used under the terms of the Creative Commons Attribution 4.0 licence. Any further distribution of this work must maintain attribution to the author(s) and the title of the work, journal citation and DOI.

P. C. H. Martens 1989). According to this model, the plasma in filaments resides in the dips of these helical magnetic field lines, and the magnetic field within the filament is of inverse polarity compared to the surrounding photospheric fields (D. H. Mackay et al. 2010). Such simulations provide valuable insights into the underlying magnetic structures that govern filament dynamics, but additional research is needed to refine these models and connect them with observational data.

Filaments are typically classified based on morphology, dynamics, and location into two groups, quiescent prominence and active prominence (N. Labrosse et al. 2010). Quiescent prominences, found at higher latitudes, are stable and can persist for weeks to months. On the other hand, active region prominences, located near sunspots, are short lived and are more prone to eruptions. Intermediate filaments bridge the gap between quiescent and active types, forming between weak background fields and active regions. Quiescent prominences can also undergo eruptions due to instabilities, leading to their classification into eruptive and noneruptive types. Moreover, the filaments are categorized based on their magnetic properties, such as helicity and chirality. The study of filament chirality can offer valuable insights into the filament's axial field direction and magnetic helicity, both of which are essential to understanding filament dynamics and eruptions.

However, determining the magnetic helicity of filaments remains a challenge due to the lack of magnetic field observations above the photosphere. The chirality of a filament is related to underlying magnetic structures. It can provide insights into the filament's axial field direction and magnetic helicity (Q. Hao et al. 2016). Filament chirality of majority of filaments can be easily determined using plenty of observations on chromospheric and coronal intensities. Researchers have developed various techniques for chirality determination. S. F. Martin et al. (1994) and S. F. Martin (1998) classified filaments as dextral or sinistral based on the direction of their axial field relative to the positive polarity side and the orientation of their barbs. A filament is considered dextral if the axial field points rightward when viewed from the positive polarity side, while sinistral filaments have axial fields directed leftward. Barbs are classified as right bearing or left bearing based on their veering direction from the filament spine when viewed from either footpoint. This method links chirality to magnetic helicity, where dextral filaments correspond to negative helicity and sinistral filaments to positive helicity.

Further, A. A. Pevtsov et al. (2003) determined filament chirality quantitatively by measuring fractional chirality based on the orientation of individual barbs in Hα images. Similarly, S. Hazra et al. (2018) estimated chirality by counting the number of right-bearing and left-bearing barbs. This method allows chirality classification based on visual inspection of barb orientation without needing magnetic field data. However, Y. Guo et al. (2010) identified a filament with mixed left- and right-bearing barbs along its axis. The existence of a flux rope and sheared arcade in different regions of the filament's magnetic structure leads to the presence of opposite bearing sense in the same filament. However, the correlation between morphology and magnetic helicity is not always straightforward. V. Aparna et al. (2024) found that only 35% of filaments in their study matched the predicted relationship between chirality, magnetic helicity, and force-free parameters. This discrepancy suggests that additional information about the filament's magnetic structure is needed to accurately determine magnetic helicity.

In addition to chirality, the combined observations on skewness of coronal arcades associated with a filament and its bearing sense also contribute to chirality estimation. S. F. Martin (1998) used the skew of magnetic loops around the filament to assess the chirality of coronal arcades that lie on top of filaments. Left-skewed loops relative to the filament axis correspond to dextral filaments, while right-skewed loops indicate sinistral filaments. These findings were confirmed by N. C. Joshi et al. (2014), who observed left-bearing barbs in conjunction with right-skewed arcades, consistent with sinistral chirality. Furthermore, studies such as P. C. Liewer et al. (2012) determined sinistral chirality in another filament combining observations on barb orientation and magnetograms. Also, they found that prominence rotates clockwise during the eruption, as reported in A. Bemporad et al. (2011), i.e., the direction of prominence rotation during eruptions can indicate their chirality (Z. Zhou et al. 2020). These combined techniques, integrating both visual and magnetic data, allow for a more precise classification of filament chirality and its relation to magnetic helicity.

Moreover, previous studies (Y. Guo et al. 2010; P.-F. Chen et al. 2014, 2020) have revealed that the orientation of filament barbs is influenced by the underlying magnetic structures. For instance, dextral filaments with right-bearing barbs are associated with inverse-polarity filaments, while left-bearing barbs tend correspond to normal-polarity configurations. According to P.-F. Chen et al. (2014), the magnetic configuration of an inverse-polarity filament can be described by the flux rope model and that of a normal-polarity filament by the sheared arcade model. In the solar atmosphere, prevalence of inverse-polarity filaments was observed (J. L. Leroy et al. 1984). This leads to a hemisphere trend in chirality, with right-bearing barbs predominantly found in the northern hemisphere and left-bearing barbs in the southern hemisphere. An earlier study on filament chirality by A. A. Pevtsov et al. (2003) defined dextral filaments as filaments following the right-bearing sense and sinistral filaments as filaments following the left-bearing sense. However, these findings may be influenced by the inverse-polarity configuration that appears in most filaments. Therefore, determining filament chirality based purely on barb orientation can lead to erroneous conclusions without considering the underlying magnetic structure.

To better understand the magnetic structure of filaments, some studies have used an extrapolated photospheric magnetic field (e.g., Y. Guo et al. 2010), while others have modeled filament structures using MHD simulations (C. R. DeVore & S. K. Antiochos 2000; Y. Fan & T. Liu 2019). P.-F. Chen et al. (2020), however, proposed a method for estimating a filament's magnetic structure using observations of both the skewness of coronal arcades and the bearing sense of barbs together, which does not rely on computationally expensive numerical techniques. Given the weak magnetic fields in the quiet Sun region, it is often challenging to extrapolate magnetic fields accurately. Thus, this study aims to use this method to study the magnetic structure of filaments.

Filaments are dynamic structures that undergo changes in their magnetic configuration and physical properties throughout their life cycle. Continuous monitoring and analysis of filaments are essential to uncover the full extent of their

characteristics. In this study, we estimate the chirality of filaments at various stages of their evolution and track their consistency over time. Additionally, we categorize filaments based on their associated active regions, eruptive behavior, magnetic structure, and chirality. This multifaceted approach will provide a clearer understanding of filament behavior and its implications for solar activity.

The rest of the paper is organized as follows: Section 2 presents a detailed description of the data used in this study, including the sources and methods of data collection. Section 3 outlines the analysis process and discusses the results obtained from the study. Finally, Section 4 provides a summary of the key findings and concludes with the implications of the results, highlighting potential avenues for future research.

2. Observational Data

To analyze the filament chirality, we utilized data from two ground-based observatories: the Kanzelhöehe Solar Observatory (KSO) in Austria and the Global Oscillation Network Group (GONG; J. W. Harvey et al. 1996) at Cerro Tololo Inter-American Observatory (CT) in Chile. Both observatories provide full-disk Hα images with pixel resolutions of 1.″02 and 1.″0, respectively. These Hα images were instrumental in estimating the bearing sense of the solar filaments. Our analysis focused on filaments observed from 2013 December 1 to 2014 January 31 providing an adequate dataset for examining filament morphology during this period.

In addition to the ground-based Hα observations, we determined the skewness of associated coronal loops using the extreme ultraviolet (EUV) intensity data collected during the same observation period. For this, we relied on data from the Atmospheric Imaging Assembly (AIA; J. R. Lemen et al. 2011) on board the Solar Dynamics Observatory (SDO), which offers full-disk solar observations with a time cadence of 12 s. Solar filaments are observed in the SDO/AIA in EUV wavelengths of 171, 193, and 304 Å, with a pixel resolution of 0.″6. The coronal loops above the filaments are also observed in EUV wavelengths of 171, 193, and 211 Å. The examination of the coronal loops above the filaments enhances our understanding of their structure and orientation.

To identify the presence of active regions associated with filaments and to study their magnetic fields, we incorporated line-of-sight magnetic field data from the Helioseismic and Magnetic Imager (HMI) on board the SDO. The SDO/HMI provides magnetic field data with a pixel resolution of 0.″6 and a temporal resolution of 45 s. These data are crucial for analyzing the magnetic environment surrounding the filaments and their associated active regions, offering valuable insights into the relationship between filament structure and magnetic activity in the solar atmosphere.

3. Analysis and Results

We studied the properties of 35 solar filaments observed from 2013 December 1 to 2014 January 31. Initially, these filaments were identified and labeled FL01 through FL55. We tracked their evolution through multiple observations and recorded their changes over time. As we continued to track the filaments, we identified repeated observations and reassigned each filament a new label, FLM01 through FLM35, to reflect their updated status.

To better organize the filaments, we classified them into different categories based on their observed characteristics. This classification was essential for understanding the variations in filament morphology and dynamics across the observation period. Additionally, we estimated the chirality and magnetic structure of each filament, providing crucial insights into their underlying magnetic properties and their role in solar activities.

The results of our analysis, including detailed observations and categorization, are presented in Figures 1–8. A summary of the filament properties, including their morphology, chirality, and magnetic characteristic, is provided in Tables 1–2. These results offer a comprehensive view of the filaments' behavior and structure during the study period.

3.1. Bearing Sense of Chromospheric Filaments

We determined the bearing sense of filaments using the method outlined by Y. Hanaoka & T. Sakurai (2017). The left- or right-bearing orientation of a filament barb can be discovered as follows: Initially, move along the filament spine in a direction to make an acute angle with a specific barb from the direction of motion. If this barb is observed on the right side of the filament spine, it is considered right-bearing. Conversely, if this barb is observed on left side of the filament spine, it is considered left-bearing. The Hα images of filaments FLM06 and FLM28 with right-bearing barbs are shown in Figures 1(a) and (d), observed in the northern and southern hemisphere, respectively. We overlaid a schematic representation of their bearing sense in each panel. Similarly, in Figures 1(b) and (c) we displayed Hα images of filaments FLM08 and FLM22, which exhibit left-bearing barbs.

Further, we calculated fractional chirality (C_f) by considering the number of right- and left-bearing barbs, denoted as N_R and N_L, respectively. For this, we examined Hα images captured by GONG/CT and KSO. According to A. A. Pevtsov et al. (2003), the fractional chirality is given by the equation

$$C_f = \frac{N_R - N_L}{N_R + N_L}. \quad (1)$$

The detected bearing orientation and C_f value for each filament are listed in Table 1. Ambiguous cases, footnoted and excluded from the summary, highlight challenges in consistent classification due to factors like low $|C_f|$, changes in bearing/skewness, projection effects, and unclear observations. The fractional chirality (C_f) values range from −1.00 to 1.00, indicating the bearings of their barbs and their senses of twist.

Our findings indicate that filaments with right-bearing barbs are predominantly located in the northern hemisphere, while left-bearing barbs are more commonly observed in the southern hemisphere. In total, 46% of filaments exhibit a left-bearing sense in their barbs, while 40% show a right-bearing sense. The remaining 14% of filaments have erroneous chirality values.

3.2. Skewness of Coronal Arcade

We estimated the skewness of coronal arcades, which are loop structures above solar filaments. Skewness is defined in relation to the filament axis and the direction of the filament barbs, as described by S. F. Martin (1998). When viewed from above, right-skewed arcades form an angle with the filament axis in the same direction as the right-bearing barbs. Similarly, left-skewed arcades form an angle with the filament axis that

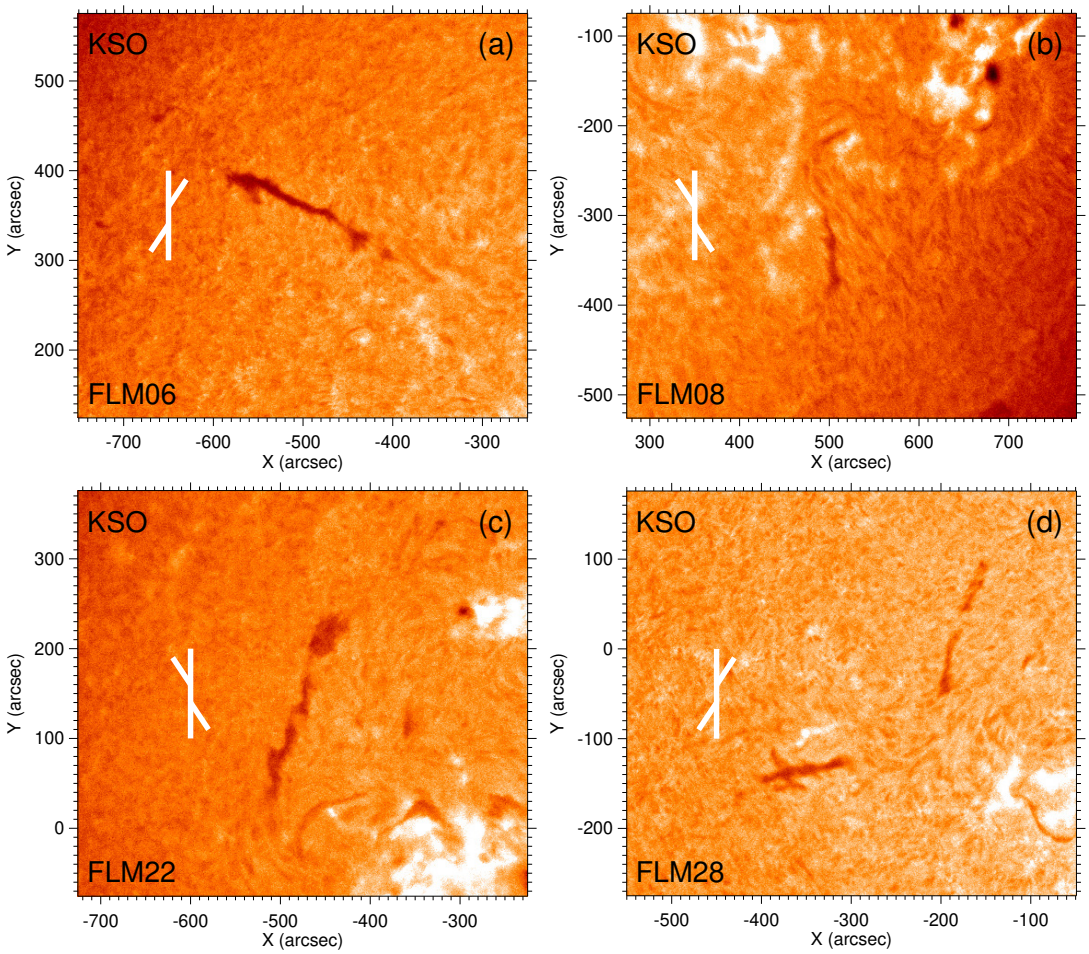


Figure 1. Hα intensity images of four filaments observed by KSO, with the white crosses in each panel representing the filament orientation.

aligns with the left-bearing barbs. Left-skewed arcades are typically found above dextral (left-handed) filaments, while right-skewed arcades are found over sinistral (right-handed) filaments.

To analyze the skewness of coronal arcades, we used EUV intensity images from the SDO/AIA observations at wavelengths of 171, 193, and 211 Å. Figure 2 shows SDO/AIA 193 Å images of coronal arcades in the region of four filaments. From these EUV images, we found that the filaments FLM06, FLM22, and FLM28 exhibited left-skewed arcades, while FLM19 displayed a right-skewed arcade. In total, we identified the skewness of coronal arcades corresponding to 20 filaments, as summarized in Table 1. However, the skewness of the coronal arcade in one filament could not be determined due to an observed change in skewness. The remaining 19 filaments adhered to the hemispheric helicity rule based on the skewness of their associated arcades.

The skewness of the coronal arcades associated with filaments varies. In total, 46% of filaments exhibit a right-skewed arcade, and 8% show a left-skewed arcade. However, for nearly half of the filaments (46%), skewness data are not available. We determined the magnetic structure of 46% of filaments through clear observations of their skewness in overlying coronal arcades. By considering filaments whose skewness is determined, the majority of filaments (87%) are associated with a flux rope morphology. A sheared arcade morphology is observed in 13% of the filaments.

3.3. Classification of Chromospheric Filaments

To identify the presence of active regions near solar filaments, we examined magnetograms from SDO/HMI and Helioviewer. Based on these observations, we identified 10 filaments associated with active regions, which were classified as active region filaments (labeled AR). Another 10 filaments were categorized as quiescent filaments (labeled QR), as they were observed in quiet regions with no sunspots. The remaining 15 filaments were intermediate filaments (labeled IF) as they were located near relatively weak active regions.

In Figure 3, we present the observations of filament FLM06 with a line-of-sight magnetogram (panel (a)), a Hα intensity (panel (b)), and EUV intensities (panels (c) and (d)) in different wavelengths. This filament is classified as a quiescent filament according to the SDO/HMI line-of-sight magnetogram in panel (a). We found three right-bearing barbs in the Hα image as shown in panel (b). The filament's plasma and its associated coronal arcade are clearly visible in SDO/AIA 304 Å and SDO/AIA 211 Å, as shown in panels (c) and (d), respectively. We observed a left-skewed coronal arcade associated with this filament classified as a dextral filament. Additionally, the observed line-of-sight magnetic field, Hα image, and EUV images in different wavelengths of the other quiescent filament, FLM19, are shown in Figure 4. The FLM19 has five left-bearing barbs and a right-skewed coronal arcade as per the observations. It is classified as a sinistral

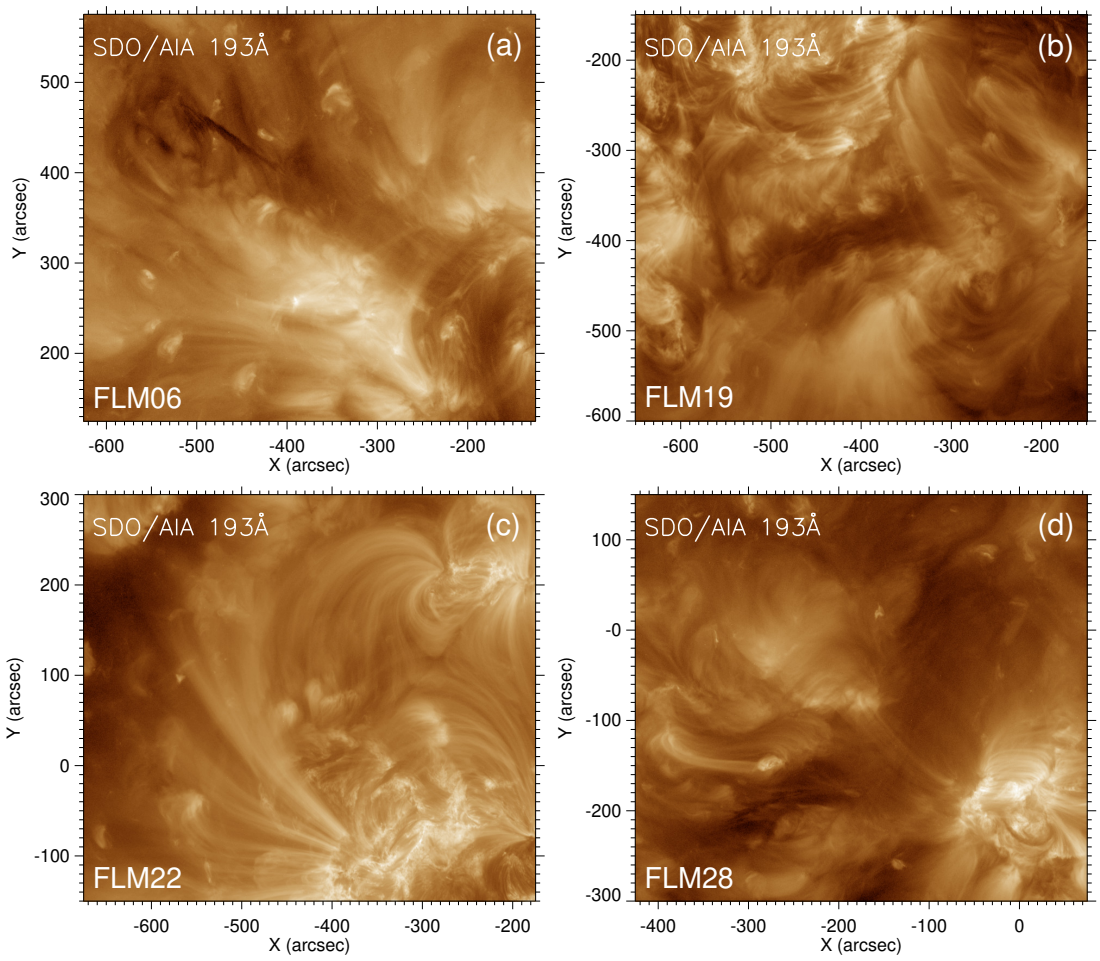


Figure 2. The SDO/AIA 193 Å intensity images of coronal arcades associated with filaments (a) FLM06, (b) FLM19, (c) FLM22, and (d) FLM28, as shown in Figure 1.

filament. On the other hand, an active region filament named FLM22 is shown in Figure 5. We found an active region at the southern footpoint of this filament, as shown in panel (a), and four left-bearing barbs in the Hα image in panel (b). The filament plasma and associated coronal arcade were clearly observed in SDO/AIA 304 Å and SDO/AIA 171 Å, as shown in panels (c) and (d), respectively. We observed a left-skewed coronal arcade associated with this filament and classified it as a dextral filament. Similarly, we determined the chirality of all filaments, and the details of these observations are tabulated in Table 1.

Throughout the observation period, we noted that some filaments underwent eruptions, prompting us to classify them as either eruptive or noneruptive. All quiescent filaments were found to be noneruptive. However, we detected one eruptive active region filament and nine eruptive intermediate filaments in our study. Regarding eruption status, the majority of filaments (71%) are noneruptive, meaning no eruption was observed during the observation period. Eruptive filaments, which are associated with solar eruptions, comprise 28% of the dataset.

In addition to this, we investigated the magnetic structure of filaments, as discussed in Section 3.4. Based on this analysis, we classified the filaments into two categories: sheared arcade and flux rope. This classification of filaments is also listed in Table 1.

3.4. Magnetic Structure of Chromospheric Filaments

We determined the magnetic structure of these filaments based on simultaneous observations of their bearing sense and the skewness of the associated coronal arcade, as described by P.-F. Chen et al. (2020). Filaments with left-skewed arcades and right-bearing barbs align with the flux rope morphology, while those with left-skewed arcades and left-bearing barbs correspond to a sheared arcade morphology. Conversely, right-skewed arcades with left-bearing barbs indicate a flux rope morphology, while right-skewed arcades with right-bearing barbs suggest a sheared arcade morphology.

To ensure an accurate determination of the filament's morphology, we analyzed each filament multiple times. We observed changes in both the bearing sense of the barbs and the skewness of the coronal arcades during the evolution of some filaments. In a few cases, the bearing sense of the barbs was unclear, leading to exclusion of these filaments from the magnetic structure analysis.

By combining observations of skewness and bearing sense, we accurately determined the morphology of 16 filaments. For example, Figure 3 shows the skewness of the coronal arcade and the bearing sense of the barbs in FLM06. It exhibits right-bearing barbs and a left-skewed arcade, which, according to P.-F. Chen et al. (2020), corresponds to flux rope morphology. In contrast, filament FLM22, shown in Figure 5, displays left-bearing barbs and a left-skewed arcade, classifying it as a

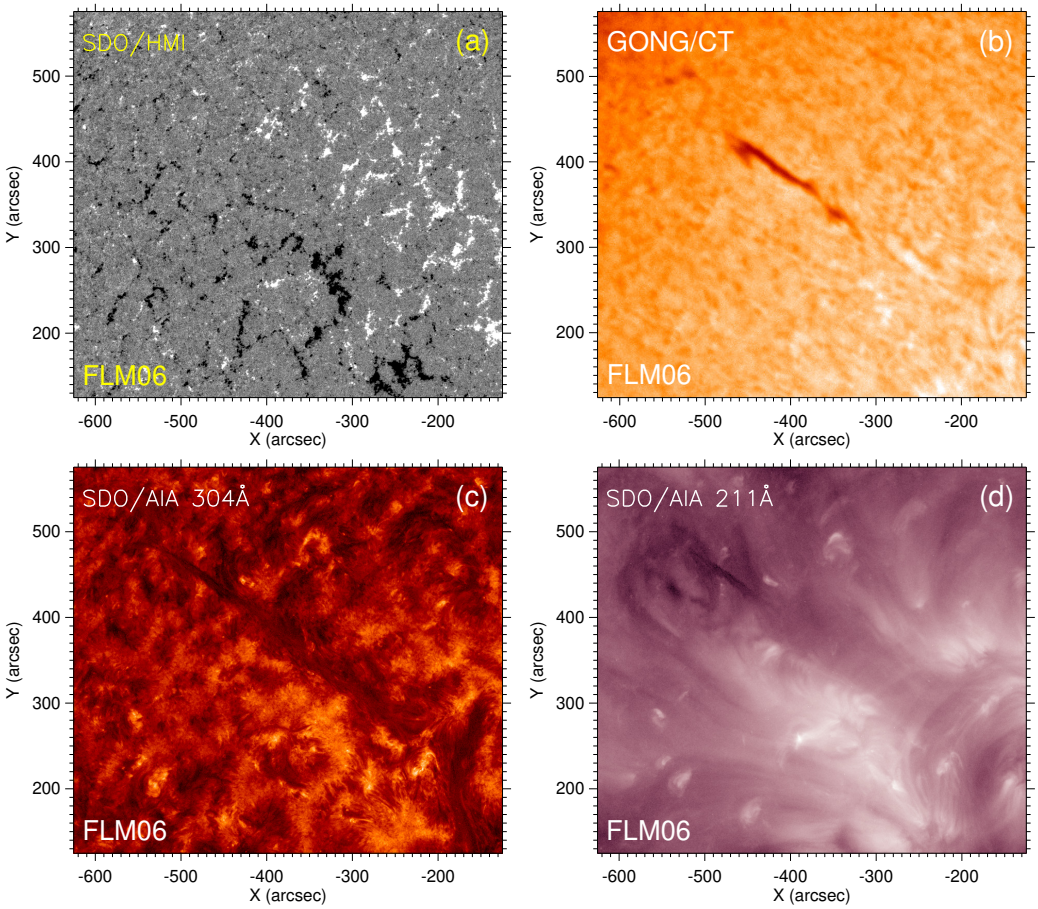


Figure 3. (a) Line-of-sight (LOS) magnetogram; (b) Hα image; (c) SDO/AIA 304 Å image; (d) SDO/AIA 211 Å image of the filament tagged as FLM06.

sheared arcade morphology. We find that 14 of the 16 filaments exhibited a flux rope morphology, while the remaining two exhibited sheared arcade morphologies. Notably, all quiescent filaments followed the flux rope morphology.

In a related study by P. T. Jain Jacob & R. A. Maurya (2025a), filament FLM33 initially exhibited a right-bearing sense. The evolution of filament FLM33 is shown in Figures 6 and 7. Filament FLM33 has two right-bearing barbs at a location ($-500''$, $-125''$) on 2014 January 20, as shown in Figure 6(b). Although the 2014 January 19 observations are affected by projection effects due to the filament's proximity to the solar limb, the observed morphology is consistent with an initial right-bearing interpretation (Figure 6(a)). However, as seen in Figure 6(b), when barbs are oriented nearly perpendicular to the filament spine, manually determining their bearing from a single Hα filtergram can be ambiguous and subject to different visual interpretations by different observers. The temporal evolution of the filament prior to its transition to a left-bearing configuration provides additional observational context supporting our interpretation. On January 21, FLM33 exhibited a transition from a right-bearing to a left-bearing configuration, where projection effects are minimal. This change in the bearing sense is summarized in Table 1. Such a change is consistent with the predominance of left-bearing filaments in the southern hemisphere. The filament is associated with active region NOAA 11959, where an enhancement in positive helicity has been reported in a recent study by P. T. Jain Jacob & R. A. Maurya (2025a). The emergence of positive helicity in the active region located at the filament footpoint is likely to influence the filament's evolution, leading it to conform to the hemispheric helicity rule. In this paper, we further examined the skewness of the coronal arcade above this filament. The observed bearing sense of filament barbs and the associated coronal arcades of filament FLM33 from January 19 to January 25 are mentioned in Table 1. These combined observations suggest that the filament underwent a magnetic structural transition from a sheared arcade to a flux rope. The evolution into a flux rope configuration is accompanied by the emergence of positive helicity from the photosphere, which is consistent with the dominant helicity in the southern hemisphere during the later stages. Throughout the observational period, the filament remained stable in the solar atmosphere. Our results indicate that the filament not only transforms into a flux rope morphology but also conforms to the hemispheric helicity rule, maintaining long-term stability in the solar atmosphere.

The bearing sense of the barbs and the skewness of the coronal arcades associated with FLM28 are shown in Figure 8. The filament consistently exhibits right-bearing barbs throughout the observations on January 13, 14 (see Figure 8(a)), and 15 (see Figure 8(c)). In contrast, the overlying coronal arcade displays a changing skewness pattern, appearing left skewed during the first observation on January 13, right skewed on January 14 (marked by a white arrow in Figure 8(b)), and left skewed again on January 15 (marked by a white arrow in Figure 8(d)). Owing to the relatively low fractional chirality present in the first observation on January 13, the inferred transition from a flux-rope to a sheared-arcade configuration

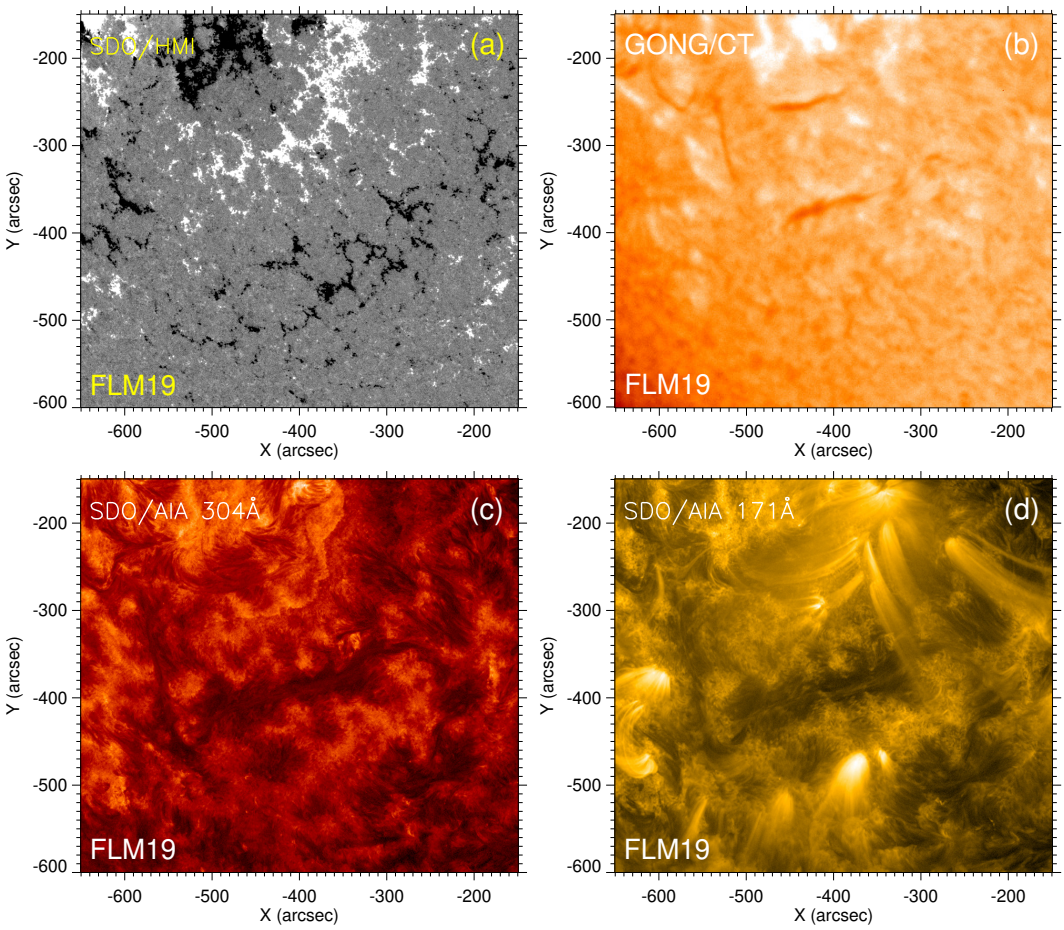


Figure 4. (a) LOS magnetogram; (b) Hα image; (c) SDO/AIA 304 Å image; (d) SDO/AIA 171 Å image of the filament tagged as FLM19.

remains uncertain. However, the subsequent evolution from a sheared arcade to a flux rope is more convincingly supported by the observed reversal in coronal arcade skewness. This filament, exhibiting a dynamically changing magnetic configuration, ultimately becomes eruptive.

The detailed morphology of all filaments is presented in Table 1. The table catalogs each filament (FLM No. and FL. No.) by date and heliospheric location (latitude and longitude). Morphological characteristics include filament type (IF, AR, and QR), eruptive nature (E/N), bearing sense of barbs (R/L), fractional chirality (C_f), skewness of the associated coronal arcade, and magnetic structure.

Table 2 summarizes the hemispheric distribution of the filaments. In total, 57% and 43% of filament observations are in the southern hemisphere and northern hemisphere, respectively. Therefore, we find that a significant portion of the filaments (53%) are left bearing, while 47% are right bearing. Additionally, 84% of filaments with arcade configurations are found in the southern hemisphere. The skewness of the associated coronal arcades reveals a clear hemispheric preference, with all arcades in the southern hemisphere exhibiting rightward skewness and those in the northern hemisphere showing leftward skewness.

4. Summary and Conclusions

We conducted a study on the morphology of several solar filaments observed during the maximum phase of solar cycle 24. During this period, a relatively large number of filaments appeared on the solar disk. Additionally, we analyzed the properties of the same filaments at different observation times, which increased the reliability of our results. We identified and merged multiple observations of the same filaments, ultimately analyzing a total of 35 filaments from an initial set of 55. These filaments were classified into three categories: quiescent, active region, and intermediate filaments. We tracked each filament to assess whether they underwent eruptions during the observation period. Furthermore, we analyzed the photospheric, chromospheric, and coronal features associated with these filaments to reveal their magnetic structures. We extended our study to investigate the characteristics of filaments exhibiting variability in their observed properties during evolution.

Using Hα intensity observations from the chromosphere, we estimated the chirality of filaments from observed orientations of their barbs. Following the approach of A. A. Pevtsov et al. (2003), we determined the filament chirality by analyzing the bearing sense of filament barbs. We found that all filaments classified as quiescent in this study are following the hemispheric chirality preference. Furthermore, 44% of active region filaments and 85% of intermediate filaments from 35 filaments also adhere to this preference, with active region filaments showing a weaker hemispheric preference compared to quiescent filaments, consistent with previous studies (A. A. Pevtsov et al. 2003). Overall, 77% of all filaments analyzed in this study, across all categories, follow the hemispheric chirality preference. Our result, corroborates

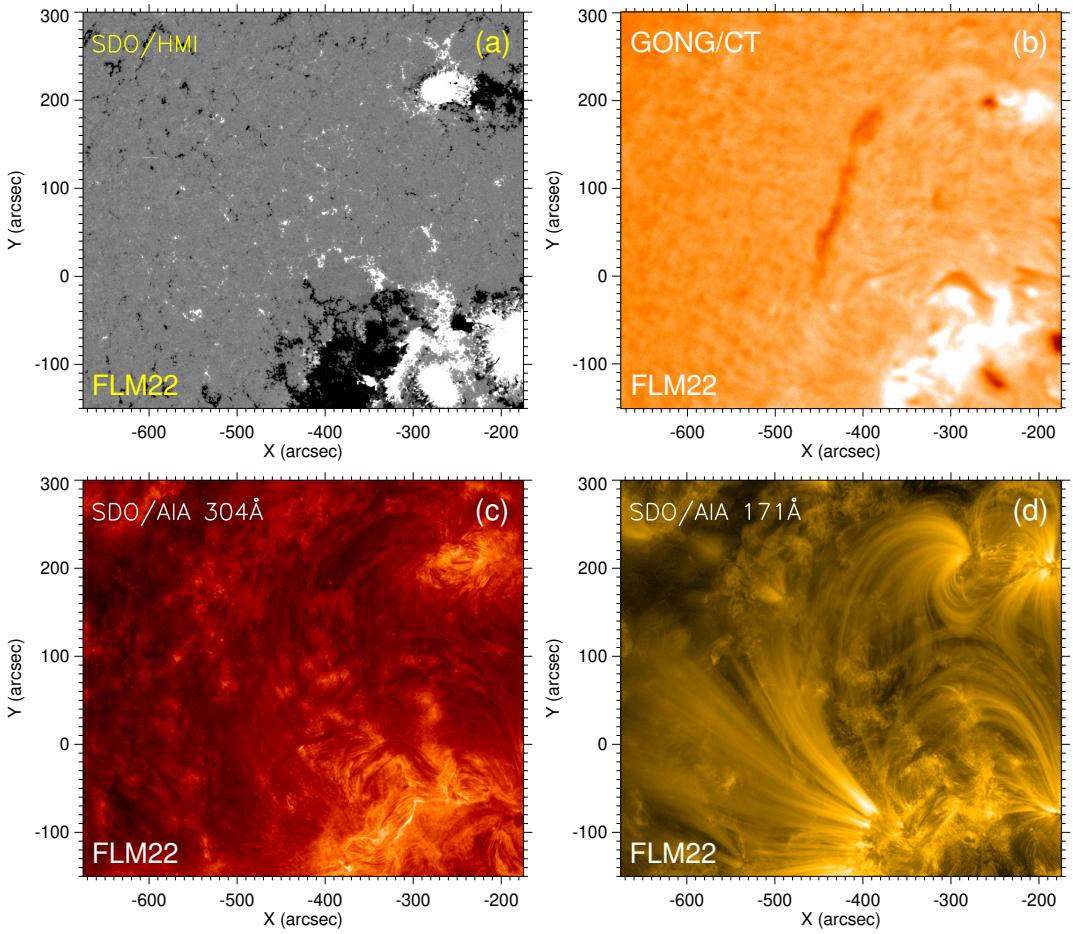


Figure 5. Observations of filament FLM22: (a) LOS magnetic field; (b) Hα intensity; (c) EUV intensity at 304 Å; and (d) EUV intensity at 171 Å.

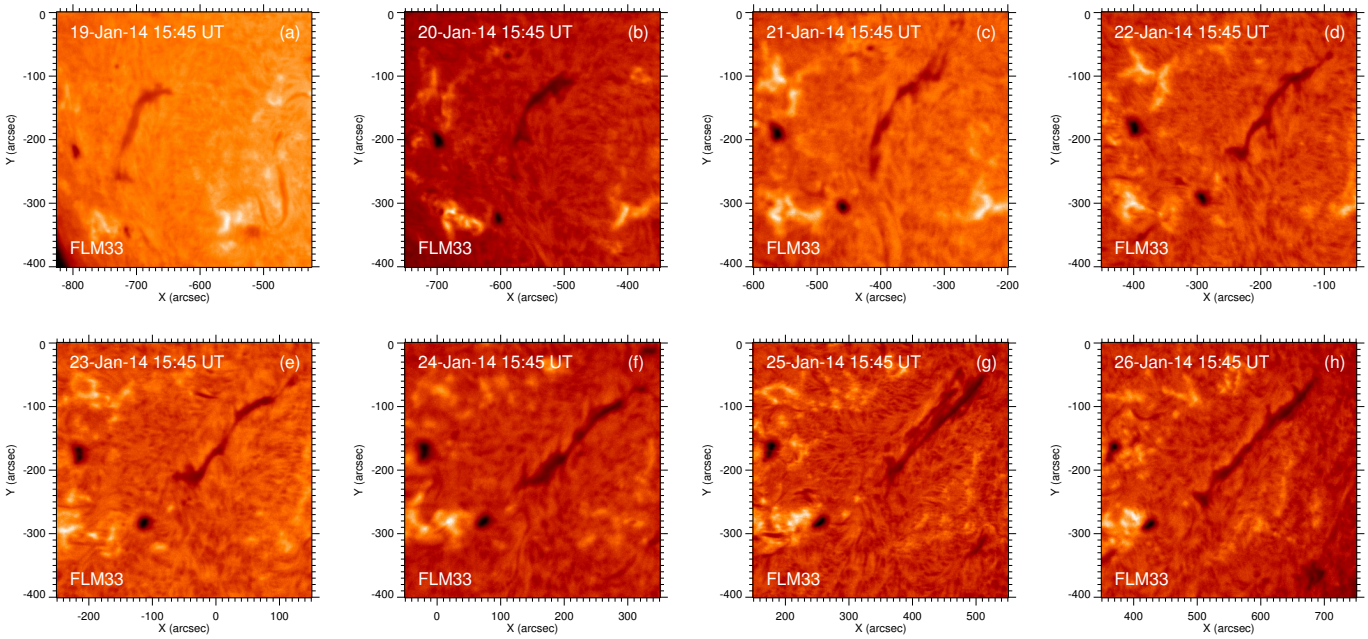


Figure 6. The GONG/CT Hα observations of the bearing sense of barbs on filament FLM33 during its evolution from 2014 January 19 to 2014 January 26.

earlier studies on filament chirality including those by A. A. Pevtsov et al. (2003) and S. Hazra et al. (2018). In addition, we evaluated eruptive nature of filaments with different chiralities and differentiated the filament chirality based on the skewness of coronal arcades associated with them (S. F. Martin 1998). Our results indicated that all filaments

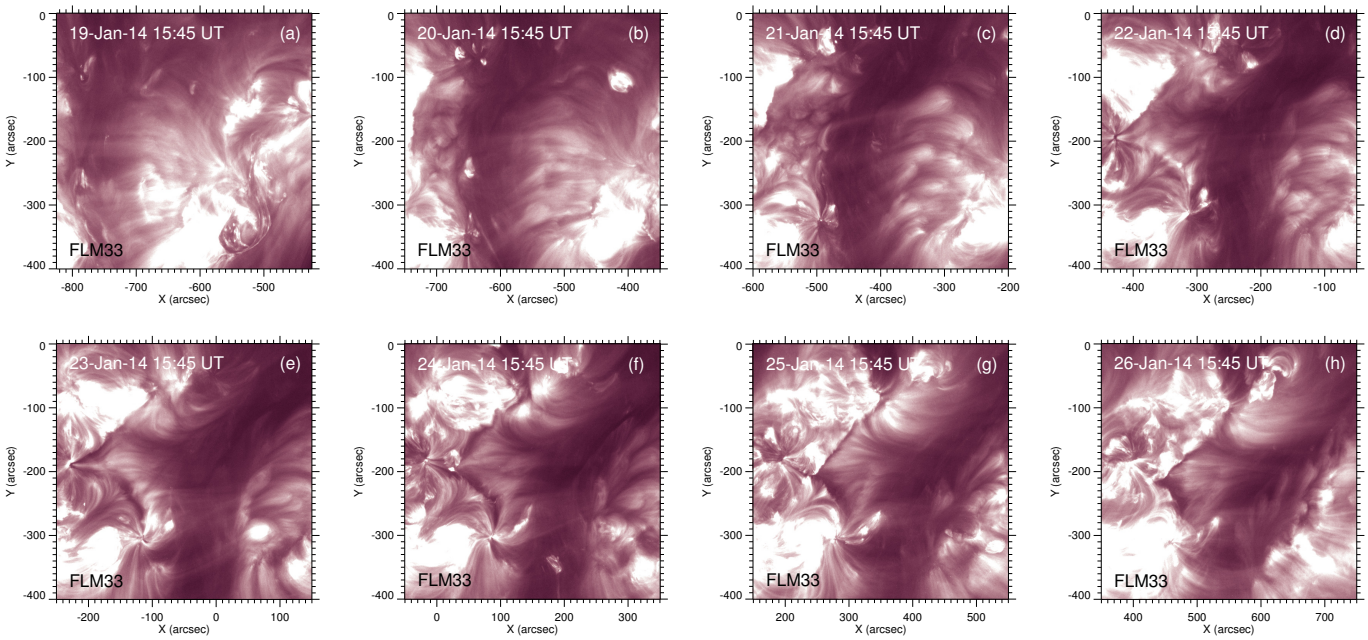


Figure 7. The SDO/AIA 211 Å observations of the skewness of the coronal arcade above filament FLM33 during its evolution from 2014 January 19 to 2014 January 26.

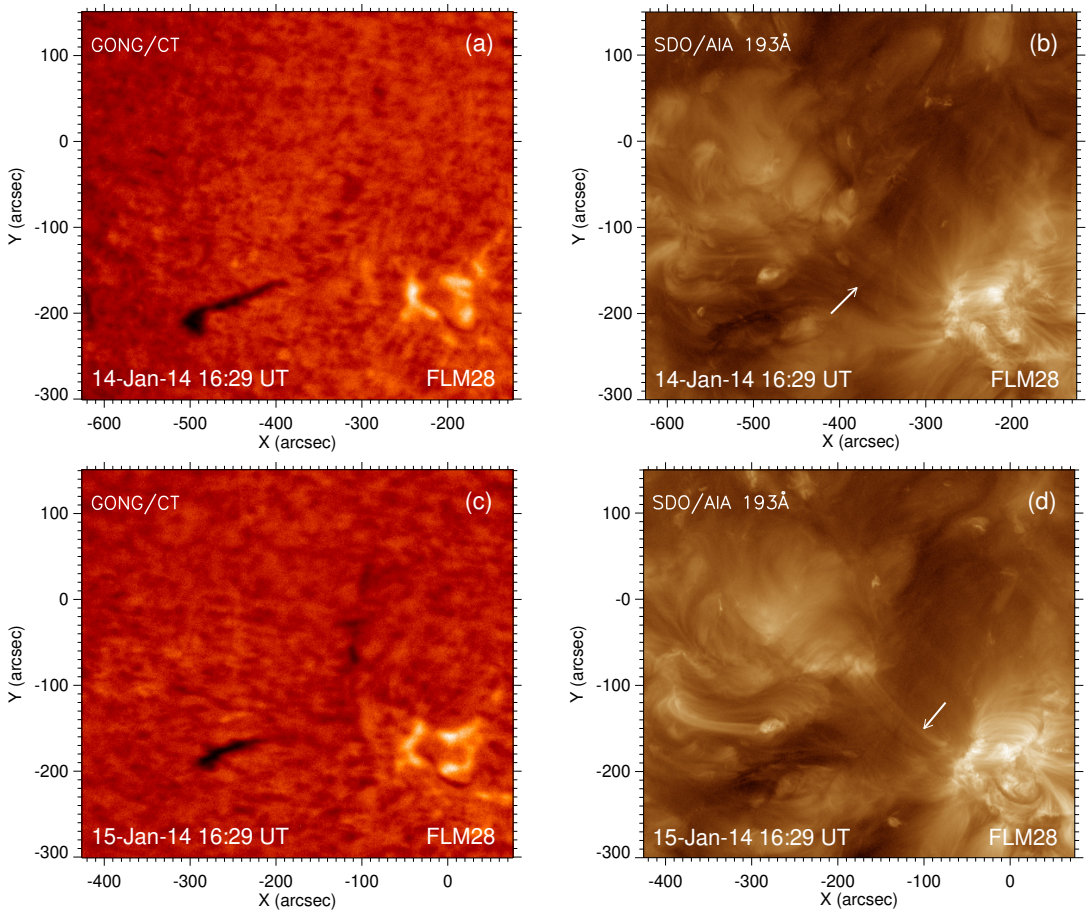


Figure 8. (a) GONG/CT Hα image and (b) SDO/AIA 193 Å image of filament FLM28 on 2014 January 14. (c) GONG/CT Hα image and (d) SDO/AIA 193 Å image of same filament on 2014 January 15. The observed coronal arcades above the filaments are marked with white arrows in SDO/AIA 193 Å images. (An animation of the filament evolution in SDO/AIA wavelength 193 Å is available in the online version.)
(An animation of this figure is available in the online article.)

Table 1
Details of Filaments' Morphology: Filament Type (F.T.), Eruptive or Noneruptive (E/N), Right- or Left-bearing (R/L), Fractional Chirality (C_f) and Skewness of the Associated Coronal Arcade

FLM. No.	FL. No.	Date	Location	F.T.	E/N	R/L	C_f	Skew.	Structure of Filament
FLM01	1	2013/12/01	(19N,35E)	IF	E	R	0.50	…	…
FLM02	2	2013/12/02	(23S,42E)	AR	...	L	−1.00	right	Flux rope
FLM03	3	2013/12/08	(29N,3W)	QR	...	R	0.50	…	…
FLM04	4	2013/12/12	(22N,33E)	QR	...	R	1.00	…	…
FLM05	5	2013/12/12	(10N,47W)	AR	...	R	1.00	…	…
FLM06[a]	6	2013/12/14	(18N,46E)	QR	...	L	−1.00	…	…
FLM07[b,c]	7	2013/12/14	(28S,51E)	QR	E	L	−0.33	…	…
FLM06	8	2013/12/16	(19N,25E)	QR	...	R	1.00	left	Flux rope
FLM07[c]	9	2013/12/16	(28S,27E)	IF	E	R	1.00	…	…
FLM08	10	2013/12/16	(26S,29W)	IF	...	L	−1.00	right	Flux rope
FLM09	11	2013/12/24	(17S,50W)	AR	...	R	1.00	right	Sheared Arcade
FLM10	12	2013/12/27	(35N,27E)	QR	...	R	1.00	…	…
FLM11[b,c]	13	2013/12/28	(1N,47E)	AR	E	R	0.33	…	…
FLM12	14	2013/12/29	(24S,44W)	AR	...	L	−1.00	right	Flux rope
FLM13[b]	15	2013/12/31	(33S,3W)	IF	E	...	0.00	right	NA
FLM14	16	2014/01/01	(29N,18E)	QR	...	R	1.00	…	…
FLM15	17	2014/01/01	(13N,40W)	QR	...	R	0.50	…	…
FLM16	18	2014/01/01	(11N,34E)	IF	...	R	1.00	…	…
FLM11[c]	19	2014/01/02	(2N,16W)	IF	E	L	−1.00	…	…
FLM17	20	2014/01/02	(7S,12W)	IF	...	L	−1.00	right	Flux rope
FLM18	21	2014/01/02	(36S,40E)	IF	E	L	−0.50	right	Flux rope
FLM19	22	2014/01/04	(26S,28E)	QR	...	L	−1.00	right	Flux rope
FLM11[a,c]	23	2014/01/04	(3N,40W)	IF	E	L	−1.00	…	…
FLM17[b]	24	2014/01/04	(7S,35W)	IF	...	L	−0.33	right	Flux rope
FLM20	25	2014/01/04	(18S,32W)	IF	...	L	−1.00	right	Flux rope
FLM21	26	2014/01/05	(22N,13E)	IF	E	R	0.50	…	…
FLM22	27	2014/01/06	(2N,25E)	AR	...	L	−1.00	left	Sheared Arcade
FLM23	28	2014/01/07	(29S,38E)	IF	E	L	−0.43	right	Flux rope
FLM19	29	2014/01/07	(26S,12W)	IF	...	L	−0.25	right	Flux rope
FLM24	30	2014/01/07	(19S,11W)	IF	...	L	−1.00	right	Flux rope
FLM22	31	2014/01/07	(3N,12E)	AR	...	L	−1.00	…	…
FLM25	32	2014/01/08	(27S,50E)	AR	...	L	−0.50	right	Flux rope
FLM26	33	2014/01/09	(22S,10W)	IF	...	L	−1.00	right	Flux rope
FLM27	34	2014/01/09	(34S,17W)	IF	E	R	0.50	…	…
FLM23	35	2014/01/09	(29S,15E)	IF	E	L	−0.50	right	Flux rope
FLM25[b]	36	2014/01/10	(26S,29E)	AR	...	...	0.00	…	…
FLM28[b]	37	2014/01/13	(12S,32E)	IF	E	R	0.33	left	Flux rope
FLM29[a]	38	2014/01/14	(20N,41W)	IF	...	R	1.00	…	…

Table 1
(Continued)

FLM. No.	FL. No.	Date	Location	F.T.	E/N	R/L	C_f	Skew.	Structure of Filament
FLM28[d]	39	2014/01/14	(15S,28E)	IF	E	R	1.00	right	Sheared Arcade
FLM28[d]	40	2014/01/15	(8S,6E)	IF	E	R	1.00	left	Flux rope
FLM30	41	2014/01/15	(8N,30W)	AR	...	L	−1.00	…	…
FLM31	42	2014/01/16	(22S,41E)	QR	...	L	−0.50	right	Flux rope
FLM32[e]	43	2014/01/18	(24N,37E)	QR	...	R	0.50	…	…
FLM33[c]	44	2014/01/19	(15S,48E)	AR	...	R	1.00	right	Sheared Arcade
FLM33[c]	45	2014/01/20	(12S,35E)	AR	...	R	0.5	right	Sheared Arcade
FLM32[e]	46	2014/01/20	(25N,15E)	QR	...	R	1.00	…	…
FLM31[b]	47	2014/01/20	(20S,8W)	QR	...	L	−0.33	right	Flux rope
FLM33[c]	48	2014/01/21	(18S,26E)	AR	...	L	−1.00	right	Flux rope
FLM31	49	2014/01/21	(22S,22W)	AR	...	L	−1.00	right	Flux rope
FLM33[c]	50	2014/01/22	(12S,11E)	AR	...	L	−0.50	right	Flux rope
FLM33[c]	51	2014/01/23	(12S,1W)	AR	...	L	−0.50	right	Flux rope
FLM33[c]	52	2014/01/24	(12S,12E)	AR	...	L	−1.00	right	Flux rope
FLM34	53	2014/01/24	(2S,23E)	AR	...	R	1.00	left	Flux rope
FLM33[c]	54	2014/01/25	(10S,29W)	AR	...	L	−1.00	right	Flux rope
FLM35	55	2014/01/25	(24S,5E)	IF	E	L	−1.00	right	Flux rope

Notes. Ambiguous results are mentioned with superscripts a–e and expansion of superscripts are mentioned in the footnote.
[a] Projection effect.
[b] Noticed low $|C_f|$ value.
[c] Noticed change in bearing sense.
[d] Noticed change in skewness.
[e] Unclear observations.

Table 2
Hemispheric Distribution of Filaments Based on Their Orientations

Filaments		North	South
		13 (43%)	17 (57%)
Bearing Sense	R	10 (77%)	4 (24%)
	L	3 (23%)	13 (76%)

having associated coronal arcades in this study follow hemispheric helicity rule according to their skewness.

The observed bearing sense of filaments depends on their magnetic structure, as highlighted earlier (P.-F. Chen et al. 2014, 2020). A dextral filament can exhibit both right- and left-bearing barbs depending on whether the underlying magnetic structure is a flux rope or a sheared arcade, respectively. We determined the magnetic structure of the filaments by combining observations of the bearing sense of their barbs and the skewness of coronal arcades above them, as mentioned in P.-F. Chen et al. (2020). While skewness data are incomplete for many filaments, right-skewed coronal arcades are more commonly observed when available. We also found that all filaments with associated coronal arcades follow the hemispheric helicity rule in this analysis. Additionally, the majority of filaments exhibited flux rope magnetic structures, as reported in Y. Ouyang et al. (2017). A clear hemispheric preference was observed, with right-bearing barbs predominantly in the northern hemisphere and left-bearing barbs in the southern hemisphere, consistent with the findings of A. A. Pevtsov et al. (2003). This observed relationship between chirality and bearing sense can be attributed to the flux rope morphology detected in most of the filaments in our study.

The evolution of a helical magnetic flux rope supporting prominence plasma has been described in earlier studies, such as A. A. Van Ballegooijen & P. C. H. Martens (1989) and C. R. DeVore & S. K. Antiochos (2000). These studies found that a sheared arcade evolves into a flux rope due to magnetic reconnection. In this study, we detected change in magnetic structure from a sheared arcade to a flux rope in two filaments during their evolution. These observations validate the results of numerical studies. We found that the majority of the filaments in our sample exhibited flux rope morphology. Moreover, we found that all the quiescent filaments in our sample were noneruptive for long time and followed the flux rope structure, indicating that flux rope morphology may be more stable than the sheared arcade configuration. However, a long lifetime does not mean that the flux rope configuration is less prone to eruption, nor does a short lifetime imply that the sheared arcade configuration is unstable. In other words, the

lifetime simply reflects the inherent characteristics of quiescent and active regions. The eruptive behavior of filaments is commonly associated with processes such as magnetic reconnection, kink instability, and flux emergence within the filament plasma structure. In this study, two filaments undergo a morphological transformation from a sheared arcade to a flux rope configuration, highlighting the dynamic evolution of a filament's magnetic structures.

The bearing sense of the filament barbs and the helicity of the associated active regions have been analyzed in P. T. Jain Jacob & R. A. Maurya (2025a). That study reports the emergence of positive helicity in the active region associated with one filament. As this filament is located in the southern hemisphere—where positive helicity is typically dominant—this may account for the observed change in barb bearing sense and its evolution into a flux rope configuration. The noneruptive nature of this filament, together with its transition from a sheared arcade to a flux rope structure, suggests enhanced stability of the flux rope morphology. A similar noneruptive behavior and morphological transition are observed in the second filament, further supporting this interpretation.

On the other hand, we identified a few filaments that exhibited changes in their bearing sense and skewness over time. In this study, we tracked the bearing sense and the skewness of the coronal arcades associated with each filament over an extended period. However, a more detailed study is required to understand the reasons for these changes and to correctly determine the chirality of filaments, as suggested by R. Chandra et al. (2009), N. C. Joshi et al. (2016), and P. T. Jain Jacob & R. A. Maurya (2025b). For example, R. Chandra et al. (2009) observed the emergence of positive-helicity magnetic clouds from active regions with negative helicity, which caused changes in the chirality of filaments. Similarly, N. C. Joshi et al. (2016) and P. T. Jain Jacob & R. A. Maurya (2025b) observed interactions between filaments with different chiralities, which resulted in magnetic restructuring of filaments during evolution.

Unlike previous statistical studies (A. A. Pevtsov et al. 2003; V. Aparna et al. 2024), where filament chirality was determined from a single observation, we tracked the filaments over time and only considered those with consistent chirality. This approach makes our chirality estimations more reliable compared to earlier studies (A. A. Pevtsov et al. 2003; V. Aparna et al. 2024; Z. Zhou et al. 2020).

In conclusion, our study provides a detailed analysis of the chirality and magnetic structure of filaments using multiple observations of the same filament over time. This approach allowed for more accurate determination of their morphology compared to previous studies. Our case study reveals that the majority of filaments exhibit a flux rope magnetic structure, supporting it as the most favorable configuration for solar filaments. Furthermore, we do not find any evidence that filaments deviating from the hemispheric chirality preference are more prone to eruption.

Acknowledgments

The data used in this paper are courtesy of NASA's SDO/AIA science team. This work also utilizes data from GONG and KSO. We thank the anonymous referees for their valuable comments and suggestions which helped us to improve the manuscript. One of the authors, R.A.M., acknowledges support from the ISRO RESPOND project (No. ISRO/RES/2/437/21-22).

ORCID iDs

P. T. Jain Jacob https://orcid.org/0009-0004-6238-1926
Ram Ajor Maurya https://orcid.org/0000-0002-6353-9252

References

Aparna, V., Georgoulis, M. K., & Martens, P. C. 2024, ApJ, 967, 134
Bemporad, A., Mierla, M., & Tripathi, D. 2011, A&A, 531, A147
Chandra, R., Pariat, E., Schmieder, B., Mandrini, C. H., & Uddin, W. 2009, SoPh, 261, 127
Chen, P.-F., Harra, L. K., & Fang, C. 2014, ApJ, 784, 50
Chen, P.-F., Xu, A.-A., & Ding, M.-D. 2020, RAA, 20, 166
DeVore, C. R., & Antiochos, S. K. 2000, ApJ, 539, 954
Fan, Y., & Liu, T. 2019, FrASS, 6, 27
Gibson, S. E. 2018, LRSP, 15, 7
Guo, Y., Schmieder, B., Démoulin, P., et al. 2010, ApJ, 714, 343
Hanaoka, Y., & Sakurai, T. 2017, ApJ, 851, 130
Hao, Q., Guo, Y., Fang, C., Chen, P.-F., & Cao, W.-D. 2016, RAA, 16, 001
Harvey, J. W., Hill, F., Hubbard, R. P., et al. 1996, Sci, 272, 1284
Hazra, S., Mahajan, S. S., Douglas, W. K., & Martens, P. C. H. 2018, ApJ, 865, 108
Jain Jacob, P. T., & Maurya, R. A. 2025a, Association between the Chirality of a Filament and the Helicity of the Supporting Active Regions (Springer), 73
Jain Jacob, P. T., & Maurya, R. A. 2025b, JGR, 130, e2024JA033479
Joshi, N. C., Filippov, B., Schmieder, B., et al. 2016, ApJ, 825, 123
Joshi, N. C., Magara, T., & Inoue, S. 2014, ApJ, 795, 4
Labrosse, N., Heinzel, P., Vial, J.-C., et al. 2010, SSRv, 151, 243
Lemen, J. R., Title, A. M., Akin, D. J., et al. 2011, SoPh, 275, 17
Leroy, J. L., Bommier, V., & Sahal-Brechot, S. 1984, A&A, 131, 33
Liewer, P. C., Panasenco, O., & Hall, J. R. 2012, SoPh, 282, 201
Mackay, D. H., Karpen, J. T., Ballester, J. L., Schmieder, B., & Aulanier, G. 2010, SSRv, 151, 333
Martin, S. F. 1998, SoPh, 182, 107
Martin, S. F., Bilimoria, R., & Tracadas, P. W. 1994, Magnetic Field Configurations Basic to Filament Channels and Filaments (Springer), 303
Ouyang, Y., Zhou, Y. H., Chen, P. F., & Fang, C. 2017, ApJ, 835, 94
Pevtsov, A. A., Balasubramaniam, K. S., & Rogers, J. W. 2003, ApJ, 595, 500
Van Ballegooijen, A. A., & Martens, P. C. H. 1989, ApJ, 343, 971
Zhou, Z., Liu, R., Cheng, X., et al. 2020, ApJ, 891, 180